

WFIRST Coronagraph: Digging Dark-Holes with Partially Corrected Pupil Phase

Erkin Sidick*, John Krist and Ilya Poberezhskiy

Jet Propulsion Laboratory, California Institute of Technology, 4800 Oak Grove Drive, Pasadena, CA 91109

ABSTRACT

The WFIRST coronagraph employs two sequential deformable mirrors to compensate for phase and amplitude errors in the coronagraph optical system. In such a system the actuators of the deformable mirrors would be used for two purposes: To flatten the overall wavefront errors at a system pupil, and to create "dark-holes". The actuators have limited stroke ranges. Therefore, if the pupil phase errors are relatively large, flattening them completely could use up a significant portion of the actuator stroke, sometimes leaving insufficient stroke for creating the dark-holes. We have investigated the impact of partially-corrected pupil phase errors on a Hybrid Lyot Coronagraph (HLC) broadband contrast performance. The predicted broadband contrast floor and the contrast chromaticity agree well with those measured on the HLC testbed.

Keywords: Coronagraphy, adaptive optics, deformable mirrors, space telescopes, exoplanets

1. INTRODUCTION

The Wide-Field Infrared Survey Telescope (WFIRST) that was recently defined to be solely a technology demonstrator also includes a visible-light coronagraph instrument (CGI) [1]. This instrument has three primary modes that rely on two different starlight suppression techniques, a Hybrid Lyot Coronagraph (HLC) [2-5] and a Shaped-Pupil Coronagraph (SPC) [6-7]. The HLC and SPC coronagraph baseline designs employ two sequential deformable mirrors to compensate for phase and amplitude errors. The actuators of the deformable mirrors would be used for two purposes: To flatten the overall wavefront errors at a system pupil, and to create "dark-holes" (or areas where the light from the star is suppressed) in a pre-selected area of the final image plane where exoplanets are expected to be found. The actuators have limited stroke ranges. Therefore, if the pupil phase errors are relatively large, flattening them completely could use up a significant portion of the actuator stroke, sometimes leaving insufficient stroke for creating the dark-holes. Using the optical model of an Occulting Mask Coronagraph (OMC) testbed at the Jet Propulsion Laboratory (JPL), we have investigated through modeling and simulations the impact of partially-corrected pupil phase errors on an HLC broadband contrast performance. In this paper we report our findings from the above studies. It should be pointed out that the current designs and the testbed of WFIRST CGI do not have the problem of large pupil phase error and insufficient actuator stroke, and we have investigated a new approach in this study to allocate more stroke for coronagraph design or relax telescope wavefront error requirements. That is, in this paper we are not presenting an existing problem, but instead proposing a new opportunity for improvement.

2. BACKGROUND

2.1 The OMC Optical System

The key elements of the OMC layout in the xz -plane is shown in Figure 1. The starlight is delivered to the OMC input pupil (Pupil-1) by a telescope. On the HLC testbed, we use a broadband light source centered at wavelength $\lambda_c=550\text{nm}$ in combination with five 2%-bandpass filters whose passbands are centered at 528, 539, 550, 561 and 572nm, respectively. In simulations, we assume the input broadband light consists of 5 monochromatic light beams whose wavelengths are equal to those listed above. A pair of 48x48 actuator deformable mirrors, DM1 and DM2, is placed in series in a shared collimated beam and forms the WFC subsystem. DM1 is located near the system pupil, and DM2 in the downstream of this pupil. They provide the control of both phase and amplitude errors in the telescope. The coronagraphic subsystem is made of just two elements, a focal-plane mask (FPM) and a Lyot-Stop. The lenses represent the powered elements in the system.

*Erkin.Sidick@jpl.nasa.gov; Phone 1 818 393-7585; Fax 1 818 393-3290; www.jpl.nasa.gov

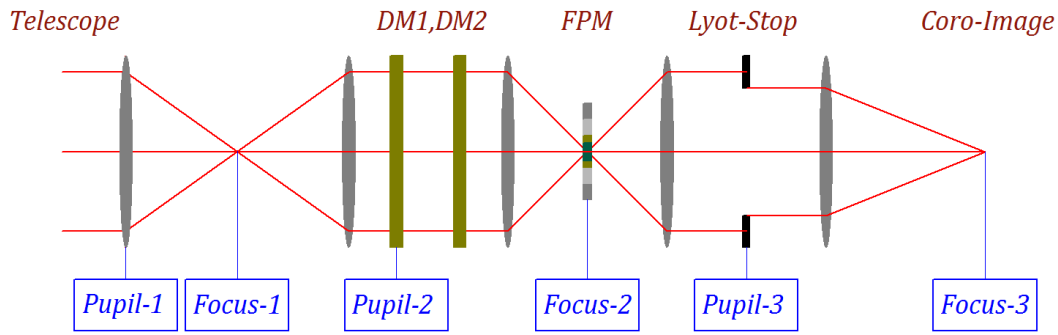


Figure 1. The key elements of the Occulting Mask Coronagraph (OMC) testbed layout. The light source (“starlight”) is a collimated beam delivered by a telescope to input pupil (Pupil-1), and a CCD science camera is located at the coronagraphic image (Coro-Image, Focus-3) plane for detecting the image of the “starlight”.

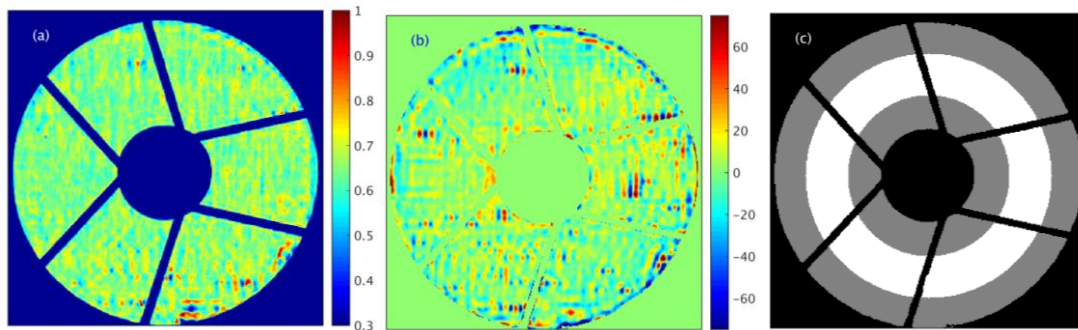


Figure 2. The WFIRST telescope obscuration pattern shown as (a) input pupil amplitude and (b) phase maps. These maps were measured at the Lyot-plane (Pupil-3 in Fig. 1) on the HLC testbed. (c) The Lyot-Stop. The WFIRST pupil, as projected to the coronagraph, is shown in black, the Lyot-Stop in gray, and the pattern of the transmitted light is in white. The phase error map in part (b) is shown as an Optical-Path Difference (OPD) map at the central wavelength of 550nm, and has the root-mean-square (RMS) and the peak-to-valley (PV) values of RMS = 16.7 and PV = 354.7nm, respectively. This map corresponds to a residual phase error obtained after flattening the total system phase errors with two DM’s.

The WFIRST telescope pupil is obscured by the secondary mirror and its six support struts. One-pair of the amplitude and the phase maps of the telescope pupil measured at the Lyot-plane of the HLC testbed is shown in Figs. 2(a) and 2(b). The phase in Fig. 2(b) is shown as an Optical-Path Difference (OPD) map at the center wavelength, $\lambda_c=550\text{nm}$, and corresponds to an HLC state after the overall system phase errors are flattened with two DM’s. The DMs are used in combination with a focal plane or an occulting mask and a Lyot plane mask, as shown in Fig. 2(c), to generate the high-contrast dark field, as well as to correct for static optical design and manufacturing imperfections and to compensate for slow thermal drift in the telescope optics. In Fig. 2(c), the WFIRST pupil, as projected to the coronagraph, is shown in black, the Lyot-Stop in gray, and the pattern of transmitted light is in white. In all of our subsequent simulations, we include a pair of “Baseline amplitude and phase maps” in our model. The amplitude is similar to the one in Figs. 2(a). For the pupil phase, we use a measured map that has not been flattened. In our compact PROPER simulation software [8, 9], it is introduced into the input pupil, or Pupil-2 in Fig. 1.

The occulting mask used in both the HLC testbed and our simulations was fabricated by depositing a reflective metal disc on a glass substrate first, then depositing a transparent dielectric layer on top of the metal layer. An atomic force microscope scan of a typical occulting mask is provided on Fig. 10 of Ref. [10].

2.2 Definitions of Normalized Intensity and Contrast

For the current optical system with two DMs, we carry out wavefront control over an annular (360-deg) dark-hole region bound by $R_{\min} = 3\lambda_c/D$ and $R_{\max} = 9\lambda_c/D$, $D \sim 48\text{mm}$ is the diameter of the input pupil aperture, $R = \sqrt{x^2 + y^2} / f$, and f is the system focal-length. We usually evaluate the contrast performance of the HLC using a normalized intensity and a contrast. The former is defined as

$$I(x, y) = I_o(x, y) / I_{uo\max}, \quad (1)$$

where $I_o(x, y)$ is the image intensity of the occulted star, and $I_{uo\max}$ is the peak value of the un-occulted star intensity. It is closely related to the contrast, the metric used most commonly in the fields of high-contrast imaging. The contrast of a field is defined as the planet-to-star flux ratio when the peak pixel of the planet's point spread function (PSF) is equal to the mean per-pixel brightness of the field [9]. We will keep track the value of one metric in this paper, the mean broadband contrast, C_{bb} . The C_{bb} is the mean value of a broadband contrast map inside an annular region from $3\lambda_c/D$ to $9\lambda_c/D$. The broadband image intensity is obtained by simply averaging the narrowband or the monochromatic light intensities at 5 different wavelengths.

2.3 WFC Algorithm and β -Value

In this paper, we use a control algorithm similar to the “minimum-wavefront and optimal control compensator” described in detail in Ref. [11]. This approach is also called “Actuator regularization” and “Electric-Field Conjugation, EFC” [12]. The WFC algorithm described in Ref. [11] uses the wavefront phase at the system exit pupil as its input, and calculates the actuator commands as its output. In the present case of EFC, we set the DM actuators to superpose the negative of the e-field onto the image plane, with a goal to make the image intensity zero on the dark-hole region on the image plane. Therefore, the WFC algorithm uses an e-field column-vector \vec{e} as its input, where

$$\vec{e} = \begin{bmatrix} \Re(\vec{E}) \\ \Im(\vec{E}) \end{bmatrix}. \quad (2)$$

The joint cost function now becomes as

$$J = \frac{1}{2} (\vec{e}^T \vec{e} + C_{wu} \vec{u}^T \vec{u}), \quad (3)$$

and the gain matrix \tilde{G} or G-matrix is obtained from

$$\tilde{G} = [\tilde{S}^T \tilde{S} + C_{wu} \tilde{I}]^{-1} \tilde{S}^T. \quad (4)$$

In Eq. (2), \vec{E} is the column-vector of the complex e-field on the dark-hole region, and in Eq. (3) the C_{wu} is the actuator regularization coefficient. \vec{E} is formed by stacking the elements of the complex e-field inside the dark-hole region in a certain order, as was explained in Eq. (1) of Ref. [11]. The $\Re(\vec{E})$ and the $\Im(\vec{E})$ are the real and the imaginary parts of \vec{E} , respectively. In Eq. (4), the \tilde{S} is the sensitivity matrix consisting of the influence functions of all actuators. It is also called “DM actuator response matrix” [9] and “Jacobian” [13]. In Eq. (3), \vec{u} is a column-vector of the actuator commands.

When operating the HLC testbed, the operator of the testbed does not have direct access to the complex e-field in the coronagraphic image-plane. Therefore, the operator does a wavefront estimation with a pairwise estimation scheme, in which “probes” are placed on one DM to modulate the electric field across the region of interest [13, 14]. Given two or more pairs of probes, along with an image with no probes at all, both the complex e-field of the residual simulated starlight and the portion of the e-field that does not interact with the probes and hence is unlikely to be correctable can be estimated (The components that do and do not interact with the probes are referred to as the “coherent” and “incoherent” parts, or “modulated” and “unmodulated” components, respectively). More details of the EFC algorithm and its testbed implementation are given in Refs. [12, 13].

Instead of C_{wu} , our testbed team at JPL prefers to use a different regularization coefficient called “ β -value”. The two coefficients are related by

$$\begin{aligned}
\tilde{\mathbf{G}} &= [\tilde{\mathbf{S}}^T \tilde{\mathbf{S}} + C_{wu} \tilde{\mathbf{I}}]^{-1} \tilde{\mathbf{S}}^T = [\tilde{\mathbf{S}}^T \tilde{\mathbf{S}} + \alpha^2 (10^\beta) \tilde{\mathbf{I}}]^{-1} \tilde{\mathbf{S}}^T \\
\rho &= \text{diag}\{\tilde{\mathbf{S}}^T \tilde{\mathbf{S}}\} \\
\alpha^2 &= \max\{\rho\}
\end{aligned} \tag{5}$$

where “diag” means “diagonal elements”, and “max” means “maximum value”. One of the advantages of this new choice is that the optimum values of β corresponding to different coronagraph configurations, such as HLC, SPC and PIAACMC, become comparable. That is, the value of α is different for different optical control systems, but the β has the same interpretation for different systems and different control iterations. In Eqn. (5), the ρ -value is an indicator of relative actuator strength. In the coronagraph studies we got involved with, the value of C_{wu} is usually positive, but the value of β is usually negative.

The simulation results to be presented in this paper exclude the errors associated with the complex e-field estimation process by obtaining the complex e-field at the final focal plane directly. The simulation creates a 1024x1024-pixel e-field at the final image plane for an aperture of ~ 305 pixels across, with ~ 3.6 pixels per $f\lambda_c/D$. Considering only the pixels in the dark-hole and 5 wavelengths gives an e-field vector, $\vec{\mathbf{e}}$, having 32,520 field pixels at $0.3\lambda_c/D$ sampling. There are a total of $48 \times 48 \times 2 = 4608$ DM actuators in the current 2-DM system, but we use only the central 3963 actuators for EFC. So $\tilde{\mathbf{S}}$ has a size of 32,520 x 3,963 pixels.

3. SIMULATION RESULTS

The pupil phase error of the HLC optical system was measured routinely by our testbed team. One of such measurement results was shown in Fig. 3(a). It has a root-mean-square (RMS) value of 105.5nm, and a peak-to-valley (PV) value of 684.1nm, respectively. If we fit 31 Zernike modes to this map, we get the Zernike coefficients shown in Fig. 3(b). We constructed a new phase map from these Zernike coefficients, and used it as the total pupil phase error in our model.

In the current case, the actuator commands can be divided into two components, that is,

$$\vec{\mathbf{u}} = \vec{\mathbf{u}}_{DH} + \alpha \vec{\mathbf{u}}_\phi, \tag{6}$$

where $\vec{\mathbf{u}}_{DH}$ is the part used to dig a dark-hole, $\vec{\mathbf{u}}_\phi$ is the part used to correct the pupil phase error, and α is a scaling factor ranging from 0 to 1. When using this approach, we include the pupil phase as it is, and use α to introduce partial correction of the pupil phase, such that $\alpha = 1$ corresponds to 100%-correction and $\alpha = 0$ to 0%-correction of the pupil phase. Figures 4(a,b) show the residual phase errors of the 100%- and 0%-correction, respectively.

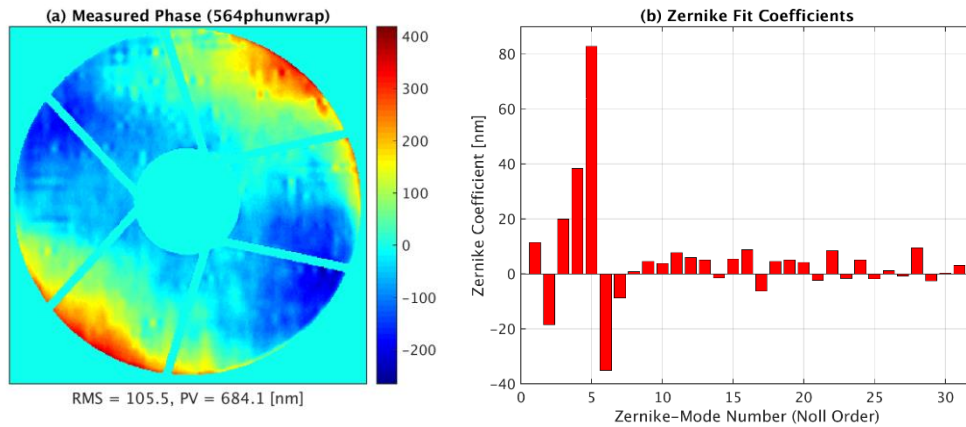


Figure 3. (a) Pre-flattening pupil phase error map and (b) its Zernike-fit coefficients. The phase map was measured with a phase-retrieval method on the OMC testbed.

Or, alternatively, we can scale the pupil phase error (Fig. 4b) between 0 and 1, and obtain the $\vec{\mathbf{u}}_\phi$ corresponding to that phase error. We followed the first approach in this paper. The PROPER model of the HLC calculates the actuator heights

in nm, and we need to convert them into actuator commands in voltages (V). We do so by using the mean values of the measured phase-flattening DM commands and the measured DM gains. Figures 5(a,b) show a pair of examples of the measured phase-flattening commands, and Figs. 5(c,d) are the examples of the measured gains of DM1 and DM2, respectively.

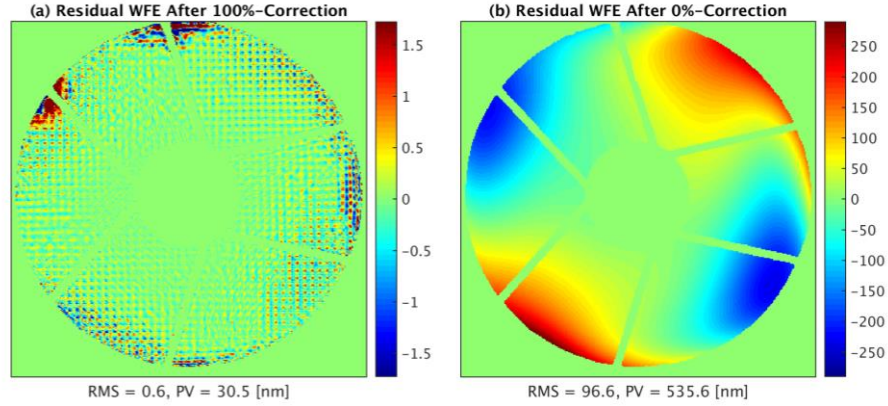


Figure 4. (a) Residual phase errors after 100% correction of the original pupil phase errors. (b) Residual phase errors after 0% correction of the original pupil phase errors. It was obtained from the Zernike coefficients in Fig. 3(b) and corresponds to the pre-control version of the phase map in part (a). The residual error maps of the 75%-corrected, 50%-corrected and 25%-corrected cases are similar in morphological feature to part (b) but have different RMS values.

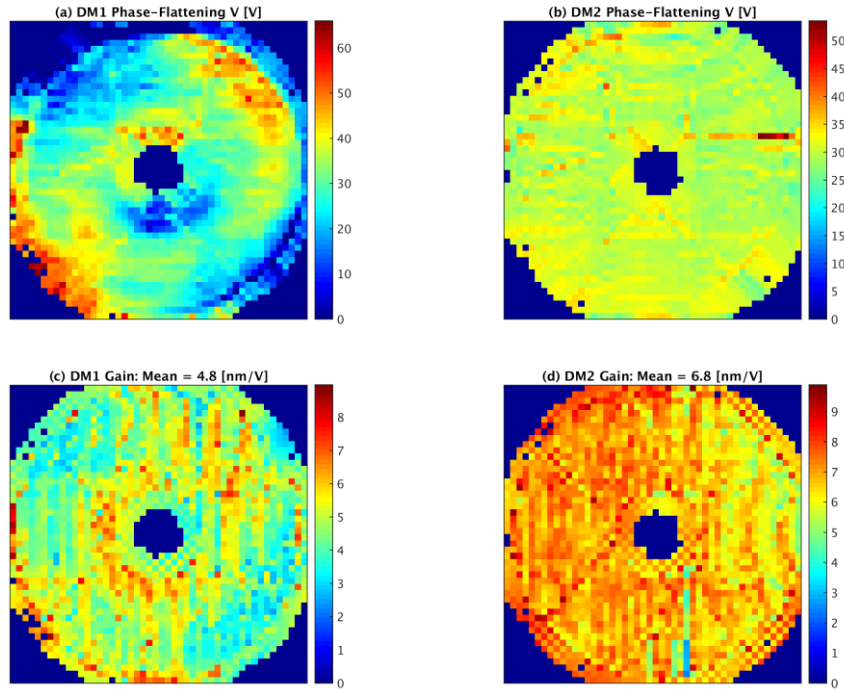


Figure 5. (a,b) Examples of the phase-flattening components of the DM1 and DM2 commands measured on the HLC testbed. (c,d) Examples of DM actuator gains measured on the HLC testbed. Only the data of the “active” actuators used in simulations are shown.

We consider five cases of pupil phase correction in this study, namely, 0%-, 25%-, 50%-, 75%- and 100%-corrections of the pupil phase. Figure 6 shows the actuator commands corresponding to the above five cases. To obtain this result, we calculated the actuator heights in nm first, converted them into voltages by dividing them with the DM1 and DM2 gains

shown in Figs. 5(c,d) next, and finally added to them the mean values of the measured phase-flattening commands shown in Figs. 5(a,b).

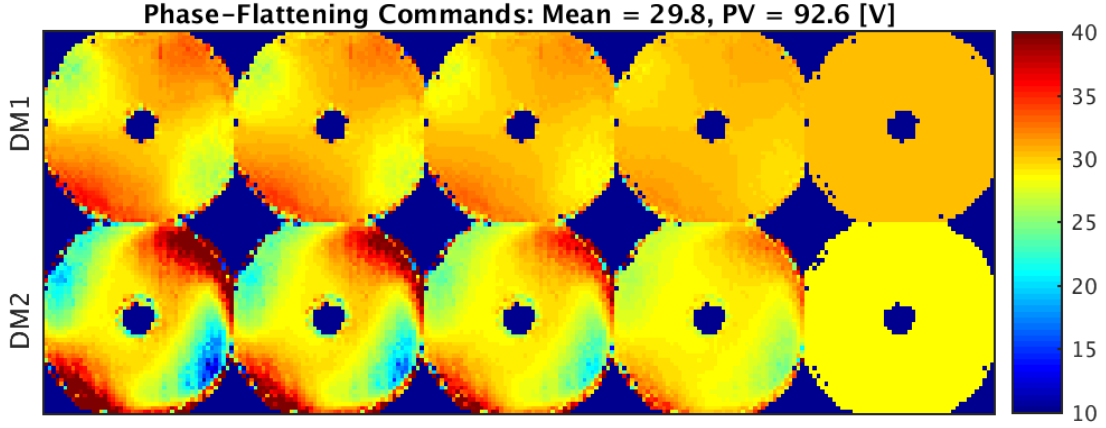


Figure 6. Phase-flattening commands of DM1 and DM2 in voltages (V). They correspond from left to right to the cases of 100%- , 75%- , 50%- , 25%- and 0%-correction, respectively. They were obtained with the following steps: (1) Obtain phase-flattening actuator heights in nm. (2) Divide them by the actuator gains in Figs. 5(c,d) to convert them into changes in actuator commands. (3) Add the mean values of the testbed phase-flattening commands given in Figs. 5(a,b) to the data obtained in Step 2.

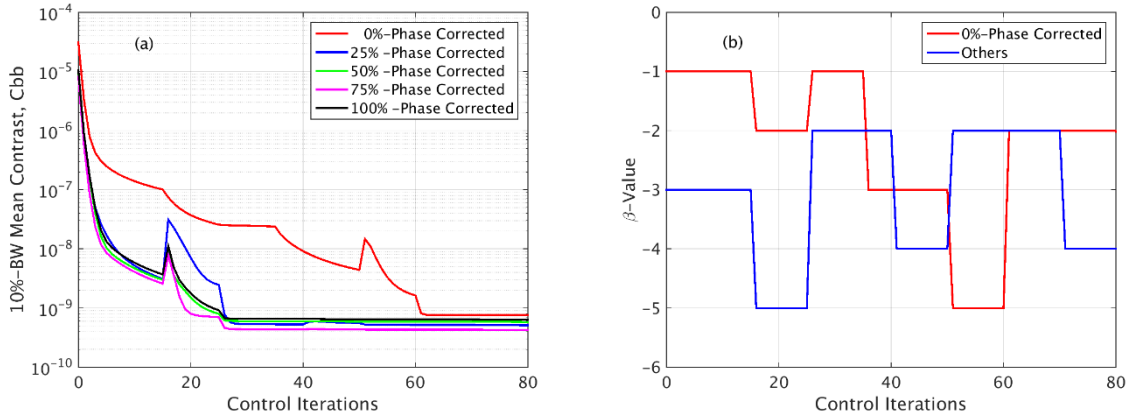


Figure 7. (a) Simulated C_{bb} -values versus control iteration number obtained without actuator constraint. Different curves correspond to the different percentages of the corrected pupil phase errors. (b) The corresponding β -values used to obtain the results in part (a).

In order to understand the impact of the partially-corrected pupil phase error on the achievable broadband contrast, we carried out EFC for the above five cases. Figure 7(a) shows the values of the mean broadband contrast, C_{bb} , as a function of control iteration number. These results were obtained without including the actuator constraints described in details in Ref. [15]. The actuator constraint consists of three parts: (1) The actuator commands must be within the 0 – 100V range. (2) Any two adjacent actuators cannot have command difference larger than 30V, or $|\Delta V| \leq 30V$. (3) Two actuators in DM1 were pegged together. Figure 7(b) shows the values of the actuator regularization factor, or β -schedule (see Ref. [16]), used to obtain the results in part (a). Figure 8 shows the predicted normalized intensities, $I(x,y)$, inside the $3 - 9\lambda_c/D$ dark-hole region corresponding to the last data points in Fig. 7(a). “100%-WFC” and “0%-WFC” mean 100%- and 0%-phase corrected, and correspond to the red- and the black-curves in Fig. 7(a), respectively.

As we can see from Figs. 7, the case of “0%-phase corrected” yields a contrast floor comparable to the other cases, but it requires a less aggressive β -schedule and as a result requires more control iterations to converge. If we use the same β -

schedule in this case as the other cases, the C_{bb} versus control iteration curve blows up. This is a major demerit of this case. Also, digging dark-hole prefers some pupil phase errors over others, and which one is preferred and which is not is completely determined by the morphology and the spatial contents of individual pupil phase maps. For example, in Fig. 7(a), the “75%-corrected” yields better contrast floor than the “100%-corrected”. Apart from the difference in surface figure or morphology, it can be expected that the “100%-corrected” phase map has much more high spatial-frequency content than the “75%-corrected”.

If we calculate the histograms of the final actuator heights, \vec{u}_{DH} , corresponding to the last points in Fig. 7(a), we obtain Figs. 9(a,b). Even though the pupil phase errors are fairly different in terms of their RMS values, the components of the DM actuator heights used to obtain the optimum contrast floors are very close to one another.

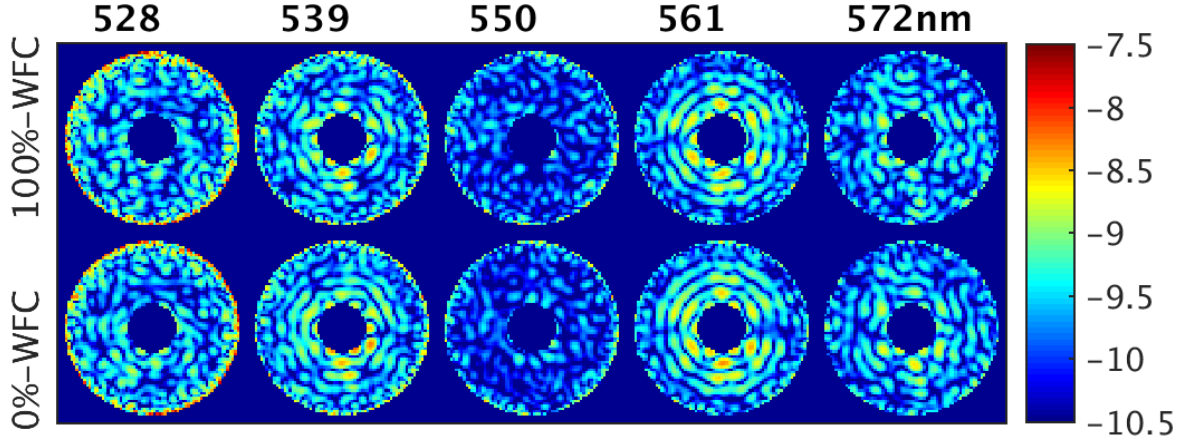


Figure 8. Examples of the predicted normalized intensities, $I(x,y)$, inside the $3 - 9\lambda/D$ dark-hole region corresponding to the last data points in Fig. 7(a). “100%-WFC” means 100%-phase corrected and corresponds to the red-curve in Fig. 7(a).

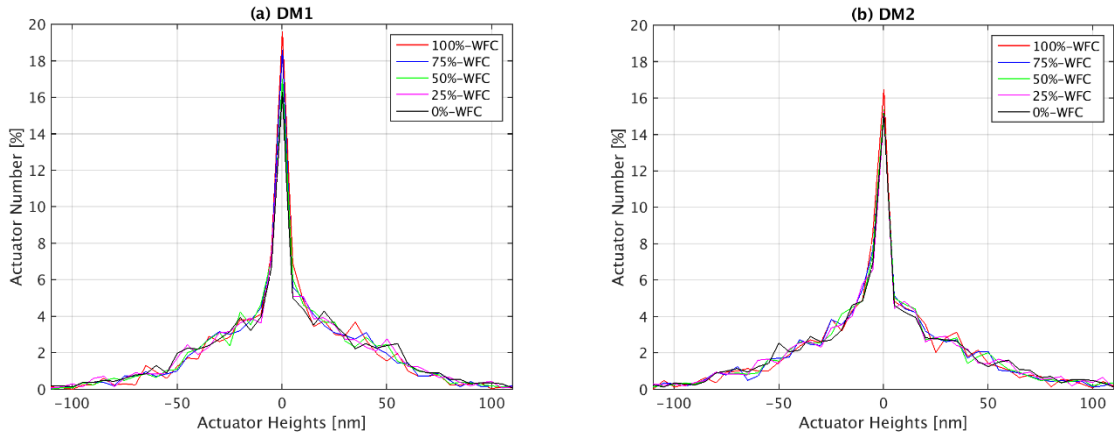


Figure 9. Histogram of the actuator heights of (a) DM1 and (b) DM2. They correspond to the last data points in Fig. 7(a) and represent the actuator strokes used to dig the dark-holes similar to and including those shown in Fig. 8.

We repeated the EFC simulations of Fig. 7(a) by including the actuator constraints in the model, and plotted the final mean broadband contrast results in Fig. 10 with a blue-curve. The red-curve are the results of the case where actuator constraints are not included in the simulations. In the same plot we also included an example of the C_{bb} values measured on the Occulting Mask Coronagraph testbed and that obtained from a baseline-model for comparison. That is, the testbed C_{bb} number is not the full CGI contrast but only the initial coherent static contrast in one polarization. In this plot, “NC” and

“WC” means “No actuator Constraint” and “With actuator Constraint”, respectively. The “Max/Min”-value is the maximum to the minimum value ratio of each curve. As we can see, when no actuator constraint is included, the contrast floor decreases by 33% in the case of the pupil phase 100%-corrected relative to the case of 0%-corrected. But such a change is a little irregular when the actuator constraint is included in the simulations, and exhibits a maximum of 59% change in the achievable contrast floor.

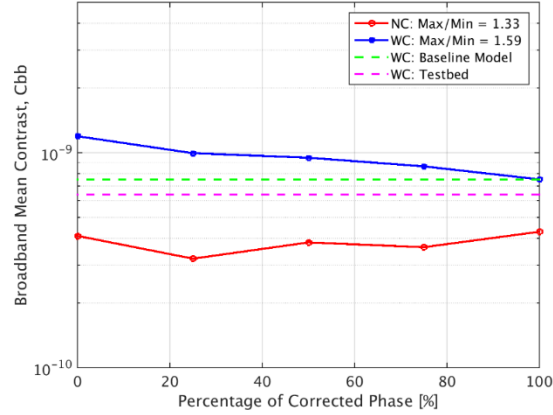


Figure 10. Mean broadband contrast floor values corresponding to different cases of pupil-phase correction. The red-curve corresponds to the last data points in Fig. 7(a). The blue-curve is the same of the red-curve except that it was obtained with the actuator constraint. A pair of C_{bb} -result examples of the baseline model and the testbed are also shown as references. “NC” and “WC” means “No actuator Constraint” and “With actuator Constraint”, respectively. The “Max/Min”-value is the maximum value to the minimum value ratio of each curve.

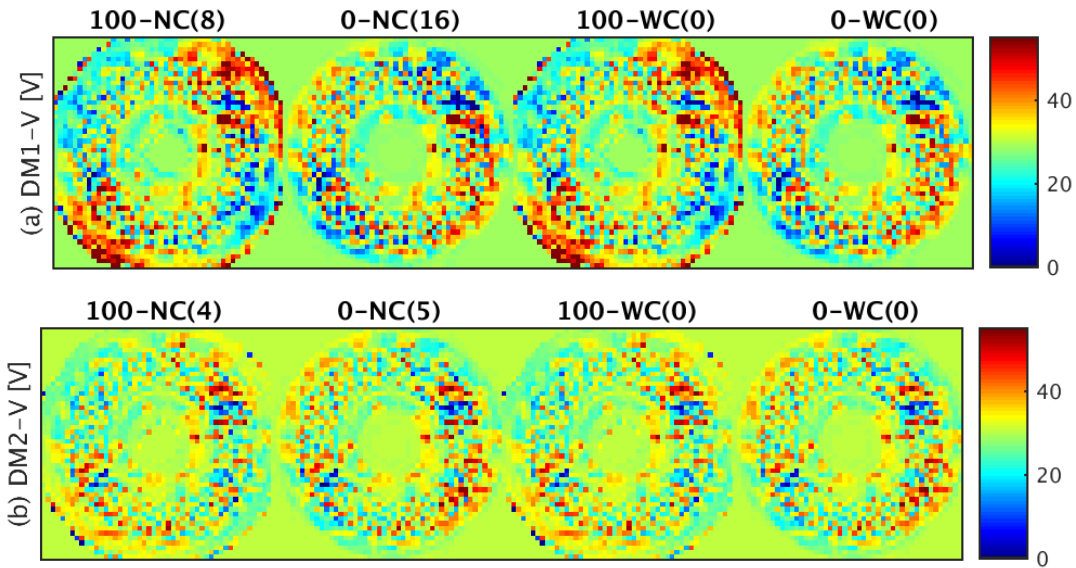


Figure 11. Total actuator commands corresponding to the cases of 100% - and 0%-phase corrected. The top- and the bottom-rows correspond to DM1 and DM2, respectively. “NC” and “WC” means “No actuator Constraint” and “With actuator Constraint”, and the number inside “(*)” are the number of actuators whose command values are outside the 0 – 100V range.

We compared the DM1 and DM2 actuator commands for the two different cases of actuator constraint and two different cases of pupil phase correction, namely, 100% - and 0%-correction, in Fig. 11. For the case of including actuator constraint, we plotted the total DM1 and DM2 actuator commands as histograms in Figs. 12(a,b). As expected, the actuator commands

spread more from their mean value when the pupil phase is 100%-corrected relative to the case of the pupil phase is 0%-corrected.

Before introducing the additional pupil phase error into the optical system, we achieved a broadband contrast floor of the green-dashed line in Fig. 10 in our baseline HLC model. The newly introduced pupil phase errors degraded that contrast floor to the levels corresponding to Iteration = 0 in Fig. 7(a), and we carried out EFC to minimize the effect of the pupil phase on the contrast floor. Such EFC process took one to 3 updated Jacobians to achieve the final contrast floors shown in Fig. 7(a).

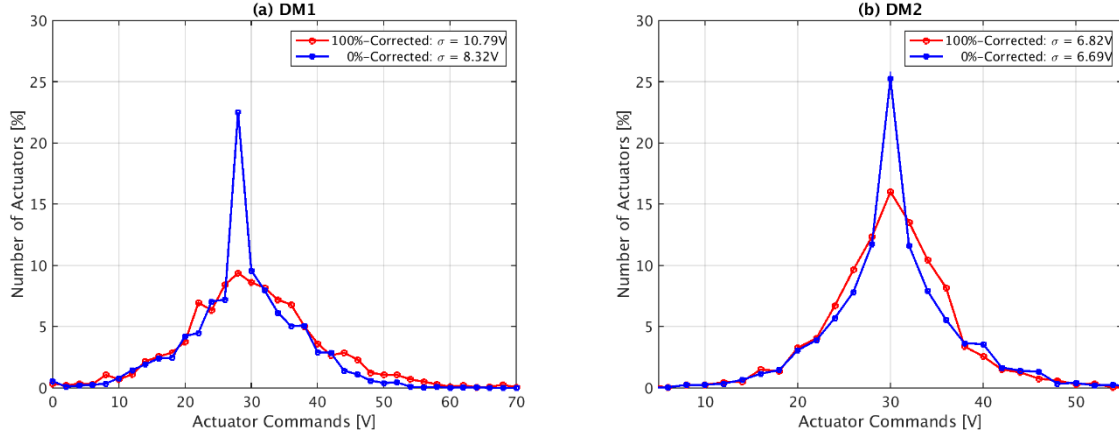


Figure 12. Histogram of the total actuator commands of (a) DM1 and (b) DM2 obtained by including the actuator constraint in EFC for two pupil-phase conditions: 100%- and 0%-phase corrected. They correspond to two data points on the blue-curve in Fig. 10(a).

4. CONCLUSION

The visible-light coronagraph instrument of the WFIRST telescope uses two separate but compatible modes, an HLC and an SPC. These two baseline coronagraph designs employ two sequential deformable mirrors to compensate for phase and amplitude errors. The actuators of the deformable mirrors would be used for two purposes: To flatten the overall wavefront errors at a system pupil, and to create "dark-holes". The actuators have limited stroke ranges. Therefore, if the pupil phase errors are relatively large, flattening them completely could use up a significant portion of the actuator stroke, sometimes leaving insufficient stroke for creating the dark-holes. In this paper we demonstrated through modeling and simulations that, in some cases, flattening the pupil phase only partially can yield contrast floors comparable to the one achieved by fully flattening the pupil phase. The results of this investigation will help us optimize CGI wavefront control strategy while conserving deformable mirror stroke range.

The jitter sensitivity of an HLC and an SPC with partially corrected pupil phase relative to those with fully flattened one has not been investigated in this paper. We will investigate how a partially-controlled pupil phase affects EFC including tip/tilt control in the future.

The research was carried out at the Jet Propulsion Laboratory, California Institute of Technology, under a contract with the National Aeronautics and Space Administration. The decision to implement the WFIRST mission will not be finalized until NASA's completion of the National Environmental Policy Act (NEPA) process. This document is being made available for information purposes only.

REFERENCES

- [1] Kasdin, N. Jeremy, et al. "The WFIRST coronagraph instrument: technology demonstration and science potential," Proc. SPIE 10698-87 (2018).
- [2] John Trauger, Dwight Moody, Brian Gordon, "Complex apodized Lyot coronagraph for exoplanet imaging with partially obscured telescope apertures," Proc. SPIE 8864, 886412 (2013).

- [3] John Krist, "End-to-end numerical modeling of AFTA coronagraphs," Proc. SPIE 9143, 91430V (2014).
- [4] Byoung-Joon Seo, *et al*, "Hybrid Lyot coronagraph for wide-field infrared survey telescope-astronomy focused telescope assets: Occulter fabrication and high contrast narrowband testbed demonstration," metrics," J. Astron. Telesc. Instrum. Syst. 2(1), 011019 (2015).
- [5] John Trauger, Dwight Moody, John Krist, and Brian Gordon, "Hybrid Lyot coronagraph for WFIRST-AFTA: coronagraph design and performance metrics," J. Astron. Telesc. Instrum. Syst. 2(1):011013 (2016).
- [6] A. Carlotti, N.J. Kasdin, and R. Vanderbei, "Shaped pupil coronagraphy with WFIRST-AFTA," Proc. SPIE 8864, 886410 (2013).
- [7] Eric Cady, *et al*, "Demonstration of high contrast with an obscured aperture with the WFIRST-AFTA shaped pupil coronagraph," J. Astron. Telesc. Instrum. Syst. 2(1):011004 (2015).
- [8] Olivier Guyon, "Imaging Earth-like planets around late-type stars with low-inner working angle PIAA coronagraphy," Proc. SPIE 8864, 886414 (2013).
- [9] John Krist, Bijan Nemati, and Bertrand Mennesson, "Numerical modeling of the proposed WFIRST-AFTA coronagraphs and their predicted performances," J. Astron. Telesc. Instrum. Syst. 2(1):011003 (2016).
- [10] F. Shi, *et al*, "Low order wavefront sensing and control for WFIRST Coronagraph," Proc. SPIE, vol. 9904, pp. 990418, August 2016.
- [11] Erkin Sidick, Scott A. Basinger, and David C. Redding, "An improved wavefront control algorithm for large space telescopes," Proc. SPIE, **7015**, 70154P (2008).
- [12] Amir Give'on *et al*, "Broadband wavefront correction algorithm for high-contrast imaging system," Proc. SPIE, **6691**, 66910A (2007).
- [13] Eric Cady, *et al*, "Demonstration of high contrast with an obscured aperture with the WFIRST-AFTA shaped pupil coronagraph," J. Astron. Telesc. Instrum. Syst. 2(1):011004 (2015).
- [14] A. Give'on, B. D. Kern, and S. Shaklan, "Pair-wise, deformable mirror, image plane-based diversity electric field estimation for high contrast coronagraphy," Proc. SPIE 8151, 815110 (2011).
- [15] Erkin Sidick, Byoung-Joon Seo, Brian Kern, Ilya Poberezhskiy, Bijan Nemati, John Trauger, "Sensitivity of WFIRST coronagraph broadband contrast performance to DM actuator errors," Proc. SPIE, SPIE Conference Paper 10400-6, August 2017.
- [16] Erkin Sidick, Byoung-Joon Seo, Brian Kern, David Marx, Ilya Poberezhskiy, and Bijan Nemati, "Optimizing the Regularization in Broadband Wavefront Control Algorithm for WFIRST Coronagraph," Proc. SPIE, vol. 10400, vol. pp.1040022-1, August 2017.